CrossMark

Mechanochemical synthesis and in vitro studies of chitosan-coated InAs/ZnS mixed nanocrystals

Zdenka Bujňáková[1,*], Erika Dutková[1], Anna Zorkovská[1], Matej Baláž[1], Jaroslav Kováč Jr.[2], Martin Kello[3], Ján Mojžiš[3], Jaroslav Briančin[1], and Peter Baláž[1]

[1] Institute of Geotechnics, Slovak Academy of Sciences, Watsonova 45, 04001 Košice, Slovakia
[2] Institute of Electronics and Photonics, Slovak University of Technology, Ilkovičova 3, 81219 Bratislava, Slovakia
[3] Faculty of Medicine, P. J. Šafárik University, 04011 Košice, Slovakia

ABSTRACT

In this paper, InAs/ZnS mixed nanocrystals were synthesized by dry high-energy milling approach in the first step. The obtained nanocrystals were characterized from structural point of view by X-ray diffraction analysis and Raman spectroscopy, and from the morphological point of view by scanning electron microscopy. In the next step, the nanocrystals were subjected to wet ultra-fine milling in order to obtain a nanosuspension of chitosan-coated InAs/ZnS nanocrystals with bio-imaging properties. The stability of the nanosuspension was examined by zeta potential and particle size distribution measurements. The prepared nanosuspension was stable with high values of zeta potential. Its optical properties were also studied using UV–Vis and PL spectroscopies. The determined fluorescent properties confirming the potential in bio-imaging applications were verified on cancer cell lines Caco-2, HCT116, HeLa, and MCF7.

Introduction

Indium arsenide (InAs) is known for its excellent electron transport properties, such as high bulk mobility, small effective mass, and low ohmic contact resistivity. Moreover, the band gap of InAs nanocrystals is size-tunable through the near-IR spectral region [1]. These properties have led to their applications in optical imaging, hologram recording, electro-optical information storage devices, and optical mass memories.

The band gap of InAs is 0.354 eV. Its combination with another inorganic semiconductor with a wider band gap can lead to even better optical properties. Therefore, in recent years, InAs nanocrystals have also been applied for biological imaging, when combined with another semiconductor [e.g., (InAs)ZnSe and (InAs)ZnCdS (core) shell quantum dots [2, 3]]. Also, zinc sulfide (ZnS) (with the band gap 3.54 and 3.91 eV for cubic and hexagonal structures, respectively) was applied. The successful synthesis of (InAs)ZnS (core)shell structure was documented in paper [4]. Subsequently, these quantum dots were coated with

🙋 Springer

Figure 1 Chemical formulas of **a** chitin, **b** chitosan.
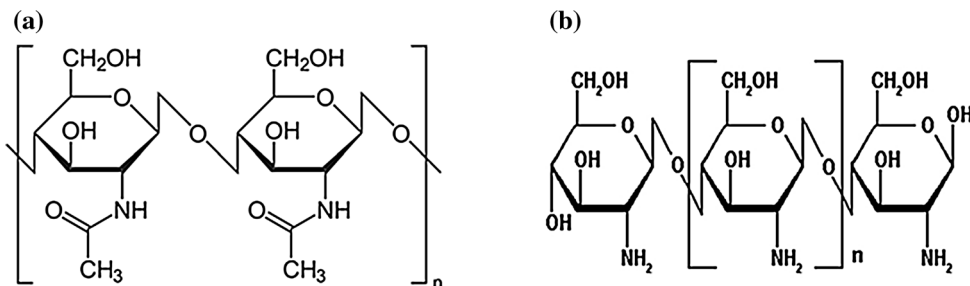
the biocompatible polymer polyethylene glycol (PEG). The authors obtained tissue and organ-selective bio-distribution using this highly fluorescent semiconductor material. The properties of InAs/ZnS nanomaterial were also described in a book [5].

When using inorganic nanocrystals for bio-imaging applications, it is necessary to cover them by organic, biocompatible material. In a plethora of available alternatives, chitosan has been often chosen because of its many advantages. The source of chitosan is a naturally occurring polymer, the chitin, which is the second most abundant polysaccharide (after cellulose) [6]. Chitosan is a nontoxic, polycationic polymer that has been broadly used in pharmaceuticals, drug carriers, and delivery systems [6–8]. Its chemical name is poly-β(1 → 4)-2-amino-2-deoxy-D-glucose. Both chitin and chitosan chemical formulas are depicted in Fig. 1a, b, respectively.

There are plenty of methods for the preparation of organic-coated nanomaterials including wet chemical procedure [9], sol–gel coatings [10] and wet aerosol synthesis [11]. The mechanochemical approach also has an important place in the preparation techniques, because of many advantages connected with the milling [12]. Using this method, it is possible to control and regulate the course of solid-state reactions and phase transformations. Moreover, it is possible to produce metastable and nonstoichiometric compounds [13, 14]. Another advantage in comparison with other procedures is a decrease in the number of technological stages and its easy scale-up. In the connection with the preparation of organic-coated nanomaterials using mechanochemistry, several papers have been written [15–17].

In this work, InAs/ZnS nanocrystals were prepared by dry mechanochemical synthesis in the first step. The samples were characterized from structural and morphological points of view. The second step was their biofunctionalization. It was done by the preparation of a stable nanosuspension, composed of these nanocrystals, dispersed in 0.1 % chitosan solution using a wet ultra-fine milling. The nanosuspension was studied with respect to the stability, and the interaction between InAs/ZnS nanoparticles and

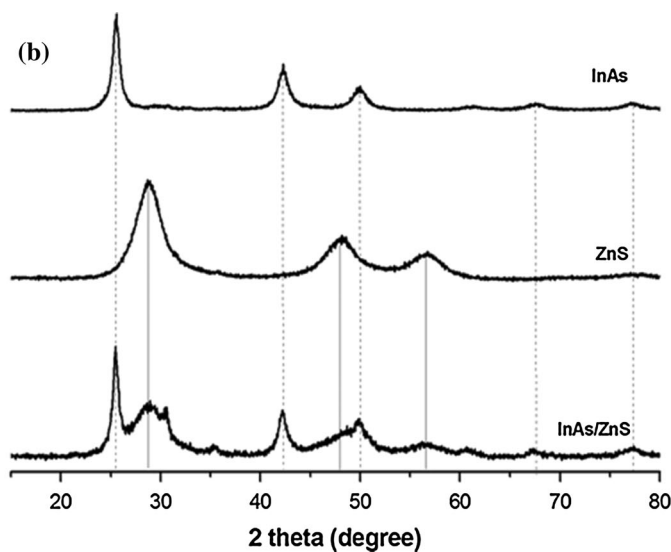**Figure 2 a** Overall scheme of InAs/ZnS nanocrystals preparation, **b** XRD patterns of InAs, ZnS, and InAs/ZnS prepared by milling.

chitosan was determined by FTIR spectroscopy. The optical properties were also studied, and the nanosuspension was tested for bio-imaging application on four cancer cell lines.

Materials and methods

Firstly, InAs was prepared by milling of elemental indium and arsenic by the procedure described in [18]. Subsequently, InAs/ZnS mixed nanocrystals were synthesized by co-milling of InAs and ZnS precursors [zinc acetate dihydrate $(CH_3COO)_2Zn·2H_2O$ (99 %, Ites, Slovakia) and sodium sulfide nonahydrate $Na_2S·9H_2O$ (98 %, Acros Organics, USA)], resulting in molar ratio InAs:ZnS = 1:4. The sample was prepared in a planetary mill Pulverisette 6 (Fritsch, Germany) in argon atmosphere for 20 min. The milling was performed in a 250 mL tungsten carbide milling chamber with 50 tungsten carbide balls, 10 mm in diameter. The rotational speed of the planet carrier was 500 rpm. After the reaction, the resulted sodium acetate was removed from the product by washing with distilled water, and after drying (70 °C, 180 min), a solid phase of InAs/ZnS was obtained. The preparation process of mixed InAs/ZnS nanocrystals is depicted in Fig. 2a and can be described by the reaction:

$$InAs + (CH_3COO)_2Zn·2H_2O + Na_2S·9H_2O \rightarrow InAs/ZnS + 2CH_3COONa + 11H_2O. \quad (1)$$
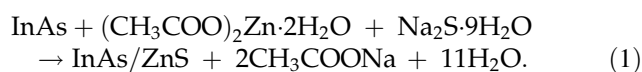
The nanosuspension was prepared in a laboratory circulation mill MiniCer (Netzsch, Germany). Five grams of InAs/ZnS sample was subjected to milling in the presence of 300 mL chitosan (high molecular weight, M(w) = 310−375 kDa, >75 % deacetylated, Sigma-Aldrich, USA) water solution (0.1 wt%) for a duration of 240 min at a milling speed 3500 rpm. The mill was loaded with yttrium-stabilized ZrO_2 milling balls, 0.6 mm in diameter. The resulting nanoparticle suspension was centrifuged at 13,000 rpm. Afterwards, the nanosuspension was characterized and stored in refrigerator (4 °C).

X-ray diffraction (XRD) measurements were carried out using a D8 Advance diffractometer (Bruker, Germany) equipped with a Θ/Θ goniometer, Cu K_α radiation (40 kV, 40 mA), a secondary graphite monochromator, and a scintillation detector. The diffraction data were collected over an angular range of $15° < 2\Theta < 87°$, with the steps of 0.03° and a counting time of 10 s/step. The commercial Diffrac^{plus} Topas has been utilized for Rietveld analyses.

Scanning electron microscopy (SEM) images were recorded using a MIRA3 FE-SEM microscope (TESCAN, Czech Republic) equipped with the EDX detector (Oxford Instrument, United Kingdom).

The particle size distribution was measured by a photon cross-correlation spectroscopy using a Nanophox particle size analyzer (Sympatec, Germany). A portion of each nanosuspension was diluted with the stabilizer-containing solution to achieve a suitable concentration for the measurement. This analysis was performed using a dispersant refractive index of 1.33. The measurements were repeated four times for each sample.

The zeta potential (ZP) was measured using a Zetasizer Nano ZS (Malvern, Great Britain). The zetasizer measures the electrophoretic mobility of the particles, which is converted to the ZP using the Helmholtz-Smoluchowski equation built into the Malvern zetasizer software. The ZP was measured in the original dispersion medium, and the measurements were repeated three times for each sample.

The FTIR spectra were recorded using a Tensor 29 infrared spectrometer (Bruker, Germany) using the ATR method.

The optical spectra were recorded using a UV–Vis spectrophotometer Helios Gamma (Thermo Electron Corporation, Great Britain) in the range of 200–800 nm.

The photoluminescence (PL) spectra at room temperature were acquired at the right angle on a photon counting spectrofluorometer PC1 (ISS, USA) with an excitation wavelength of 365 nm. A 300 W xenon lamp was used as excitation source. The emission was collected in a 25-cm monochromator with a resolution of 0.1 nm equipped with a photomultiplier.

The Raman spectra at room temperature were recorded using a MonoVista 750 CRS system, with excitation wavelengths of 325 and 488 nm.

The dissolution tests were performed by stirring 100 mg of solid phase of InAs or InAs/ZnS in 100 mL of physiological solution (0.9 % NaCl) for 30 min at 36.5 °C. The amount of dissolved arsenic was determined by atomic absorption spectroscopy method using a SPECTRAA L40/FS equipment (Varian, Australia).
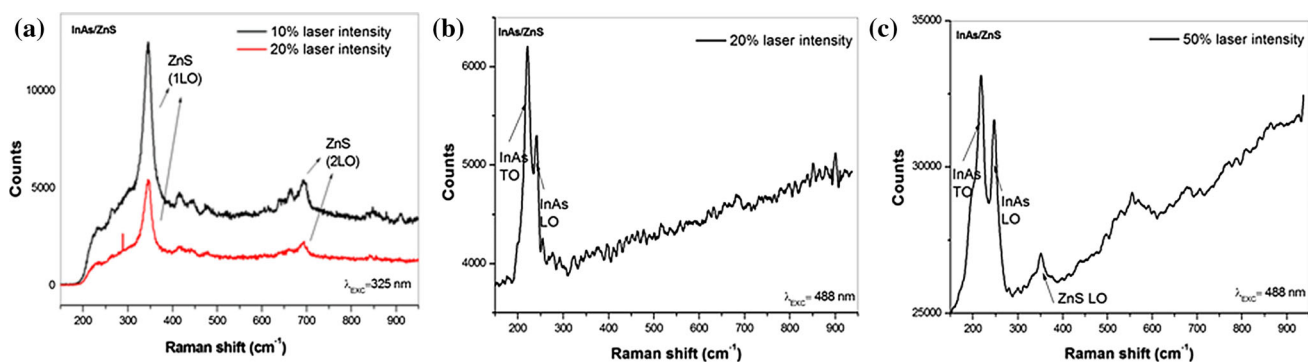
Figure 3 Micro-Raman measurements of InAs/ZnS nanocrystals at **a** 325 nm, **b, c** 488 nm with **b** 20 %, **c** 50 % laser intensity.

The human cancer cell lines HCT116 (human colorectal carcinoma) and HeLa (human cervical adenocarcinoma) were cultured in RPMI 1640 medium (Biosera, Kansas City, MO, USA). Caco-2 (human colorectal adenocarcinoma) and MCF7 (human breast adenocarcinoma) cell lines were maintained in a growth medium consisting of high glucose Dulbecco's modified eagle medium with sodium pyruvate (GE Healthcare, Piscataway, NJ, USA). Both media were supplemented with a 10 % fetal bovine serum (FBS), penicillin (100 IU/mL), and streptomycin (100 μg/mL) (all Invitrogen, Carlsbad, CA, USA) in an atmosphere containing 5 % CO_2 in a humidified air at 37 °C. The cell viability, estimated by the trypan blue exclusion, was greater than 95 % before each experiment.

The metabolic activity colorimetric assay (MTS) was used to determine the effects of InAs/ZnS nanosuspension ($c_{As} = 0.1$–1 μg/mL) on the metabolic activity of different cell lines. After 72 h of incubation, 10 μL of MTS (Promega, Madison, WI, USA) was added to each well according to the CellTiter 96® AQueous One Solution Cell Proliferation Assay protocol. After minimum of 1 h incubation, the absorbance was measured at 490 nm using the automated Cytation™ 3 Cell Imaging Multi-Mode Reader (Biotek, Winooski, VT, USA). The absorbance of the control wells was taken as 100 %, and the results were expressed as a percentage of the control. All experiments were performed in triplicate.

For the flow cytometry analyses of cell granularity, the cells were seeded at a density of 3×10^4 in Petri dishes (Sarstedt, Nümbrecht, Germany). Twenty-four hours after cell seeding, the cells were treated with InAs/ZnS nanosuspension ($c_{As} = 0.5$ μg/mL) for 72 h, washed two times with $1 \times$ PBS (Sigma-Aldrich, Great Britain), and harvested by trypsinization. The

uptake of the nanoparticles by the different cell lines was analyzed through granularity (SSC-H vs. FSC-H) changes on FACSCalibur flow cytometer (Becton–Dickinson, USA).

For cell imaging analyses, the cells (6×10^4) were seeded on 6-well plates (Sarstedt) and cultivated for 24 h in a complete medium with 10 % FBS. Afterwards, the cells were treated with InAs/ZnS nanosuspension ($c_{As} = 1$ μg/mL) for 72 h. At the end of the incubation time, the cells were washed twice in 1X PBS, fixed with 4 % paraformaldehyde, and permeabilized with 90 % methanol (Ites, Slovakia) for 20 min on ice. The nuclei were stained with SlowFade® Gold antifade reagent with 4′,6-diamidino-2-phenylindole dihydrochloride (DAPI) (Invitrogen). The slides were analyzed using Cytation™ 3 Cell Imaging Multi-Mode Reader (Biotek).

Results and discussion

Synthesis and characterization of InAs/ZnS nanocrystals

The corresponding XRD pattern, shown in Fig. 2b, gives evidence of the successful mechanosynthesis of indium arsenide, InAs (JCPDS 0-15-0869), as well as of the mechanosynthesis of zinc sulfide, ZnS (JCPDS 01-0792), from their precursors. The result of the two-step mechanosynthesis is also documented by XRD data, confirming the coexistence of both components (InAs/ZnS). The broad diffraction peaks indicate a very fine crystalline structure. Rietveld analyses of InAs/ZnS nanocrystals yielded a crystallite size $d = 45 \pm 15$ and $d = 2 \pm 1$ nm for InAs and ZnS phases, respectively. It should be noted that ZnS appeared in the resulting mixture in two
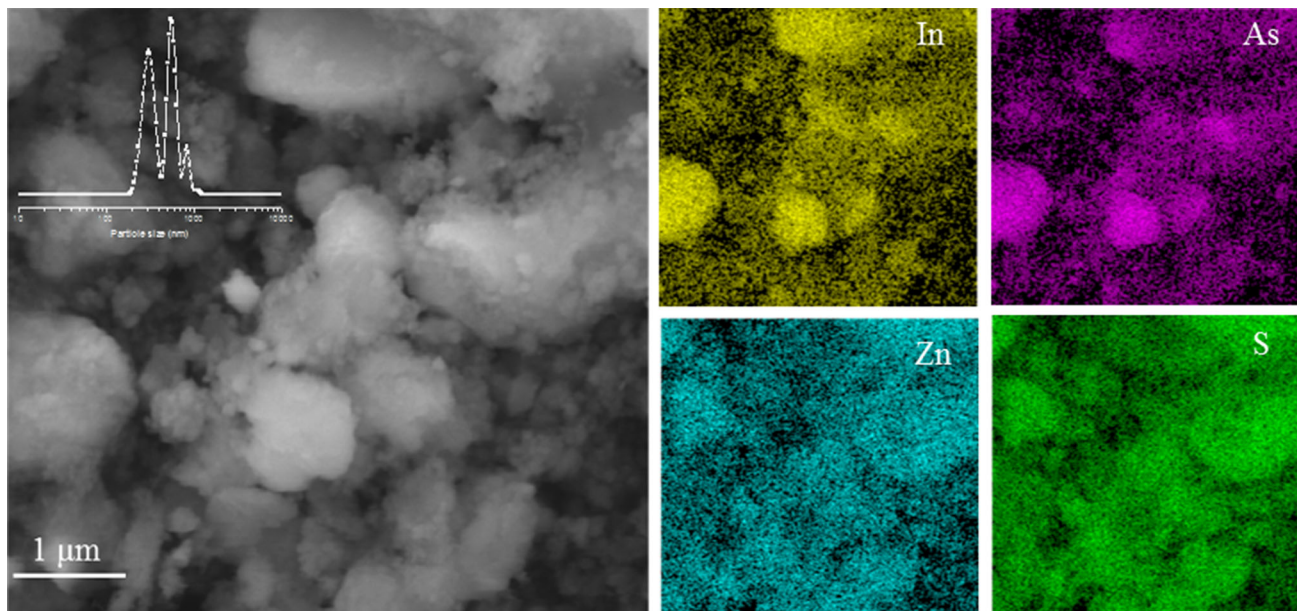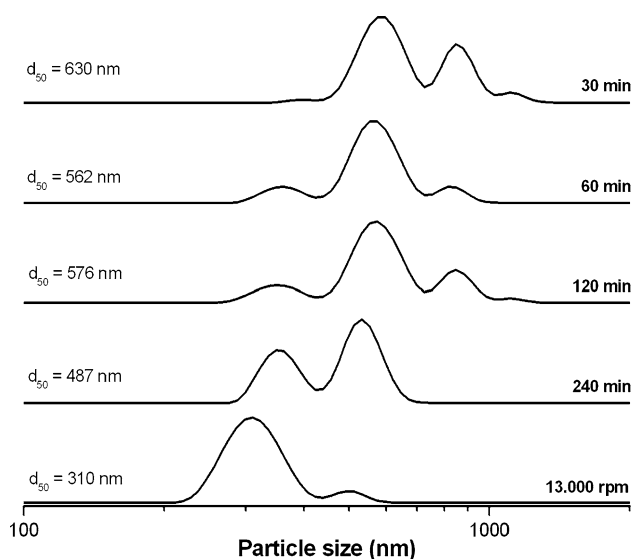
**Figure 4** SEM photographs of InAs/ZnS nanoparticles with EDX mapping and particle size distribution.

crystallographic modifications, namely as cubic sphalerite, which represents the majority of the total ZnS, and hexagonal wurtzite. According to the semi-quantitative phase analysis, the composition of the sample can be estimated as InAs—22 %, sphalerite—60 %, wurtzite—11 %, and also a small amount of In_2O_3—7 %.

The micro-Raman spectra of InAs/ZnS powder were measured in the spectral range of 100–1000 cm^{-1} at room temperature, and the results are shown in Fig. 3. Firstly, an excitation wavelength

of 325 nm was used (Fig. 3a). In this mode, only the peaks belonging to ZnS nanoparticles were observed. The intensive peak at 346 cm^{-1} is associated with the first-order longitudinal-optimal phonon (1LO) vibrational mode. The second-order (2LO) vibrational mode is located at 693 cm^{-1} [19]. The values are shifted in comparison to bulk ZnS, where for 1LO, the values from 348 to 352 cm^{-1} were identified [20–23]. In the case of 2LO, the value 673 cm^{-1} was described [22]. Further, the excitation wavelength was changed to 488 nm. At lower laser intensity (20 %), only the

Figure 5 Evolution of particle size distribution during wet ultra-fine milling of InAs/ZnS nanocrystals in chitosan.
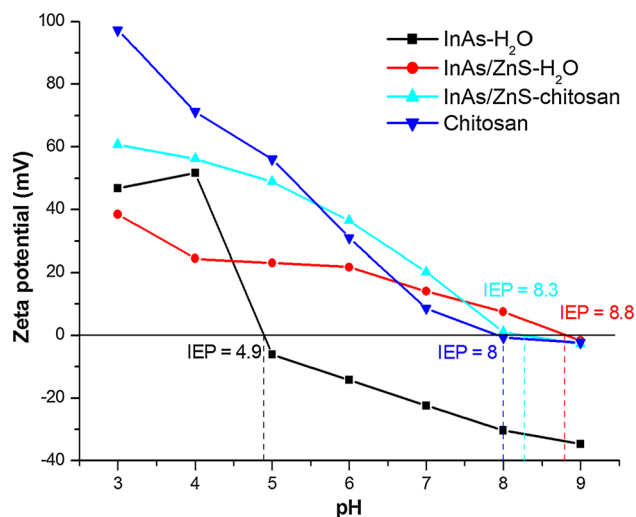
Figure 6 Zeta potential versus pH for InAs and InAs/ZnS nanocrystals measured in water and chitosan.
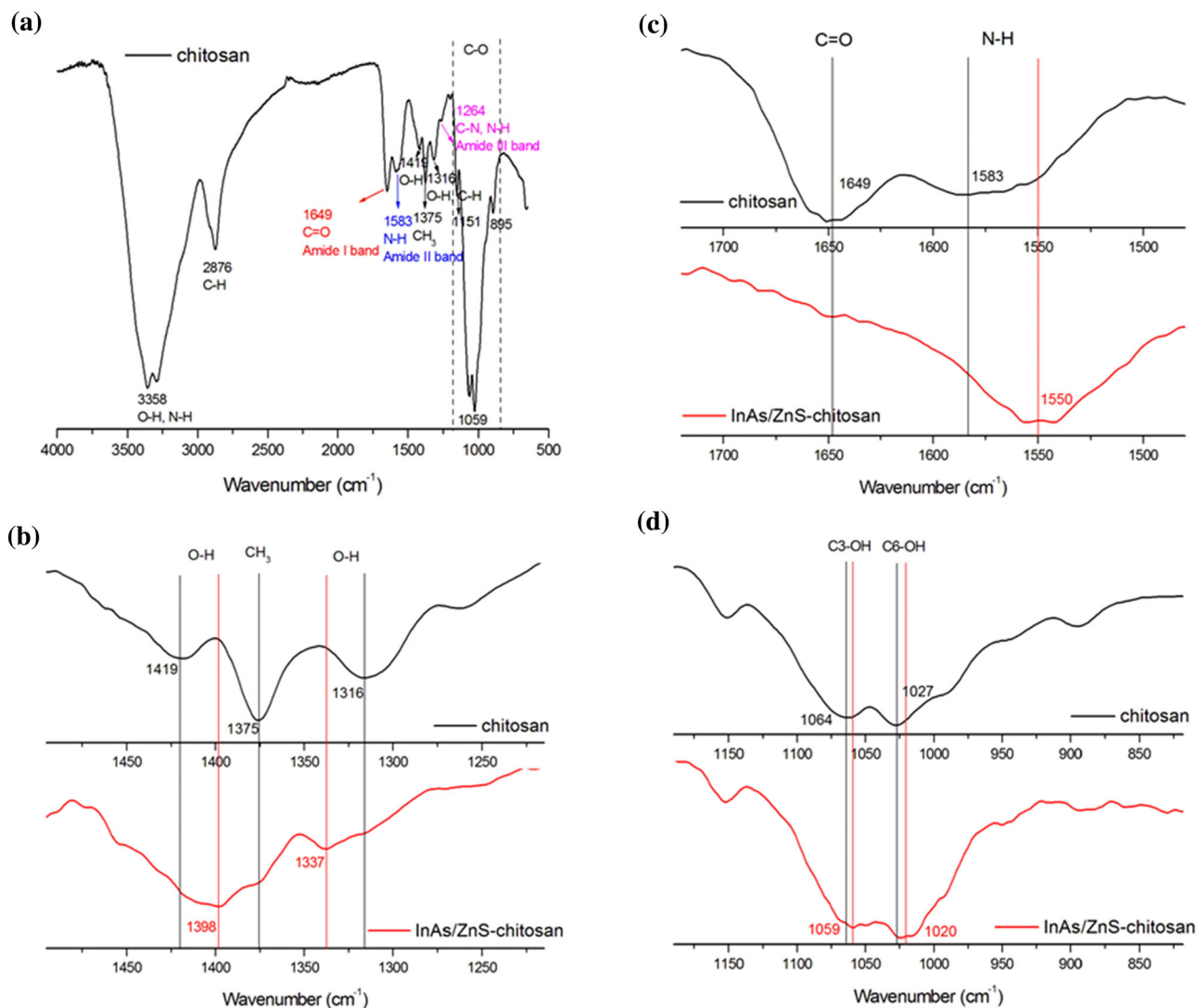
Figure 7 FTIR spectra of **a** pure chitosan, **b** hydroxyl group in a ring, **c** amide I and II bands, **d** secondary and primary alcohol vibrations. *Black lines* vibrations for pure chitosan. *Red lines* vibrations for chitosan-coated InAs/ZnS nanocrystals.

peaks corresponding to InAs nanocrystals were observed (Fig. 2b). The transverse optical (TO) frequency was found at 218 cm^{-1}, and the longitudinal-optical (LO) phonon frequency was found at 238 cm^{-1}. These values are very close to pure bulk InAs [24, 25], where 217 and 239 cm^{-1} for TO and LO, respectively, were defined. Moreover, the obtained values are shifted in comparison to our previous results (215 cm^{-1} for TO and 243 cm^{-1} for LO frequencies), in which we prepared only pure InAs nanocrystals by mechanosynthesis [18]. By increasing the laser intensity to 50 %, also the peak that attributed to 1LO of ZnS can be identified (Fig. 3c). The presence of both phases was definitely confirmed. According to [26], the phonon peak shifts

in nanostructures can be attributed to three mechanisms. Since the size of the obtained InAs nanocrystals is relatively large (45 nm), the obtained shifts can hardly be attributed only to the optical phonon confinement by the nanocrystals boundaries. While the phonon peak shifts were found from few of cm^{-1} to tens of cm^{-1}, it is supposed that the obtained shifts are due to the combination of the defects present in the structure as well as by laser-induced heating during measurement, which can be connected with the recrystallization of the sample, as higher laser intensity causes higher shifts (Fig. 3b, c).

The morphology of the mechanochemically prepared InAs/ZnS mixed particles was studied using a SEM (Fig. 4). As can be seen from the photographs,

Figure 8 Schematic representation of the possible interactions between chitosan and InAs/ZnS particles (*dot line*).
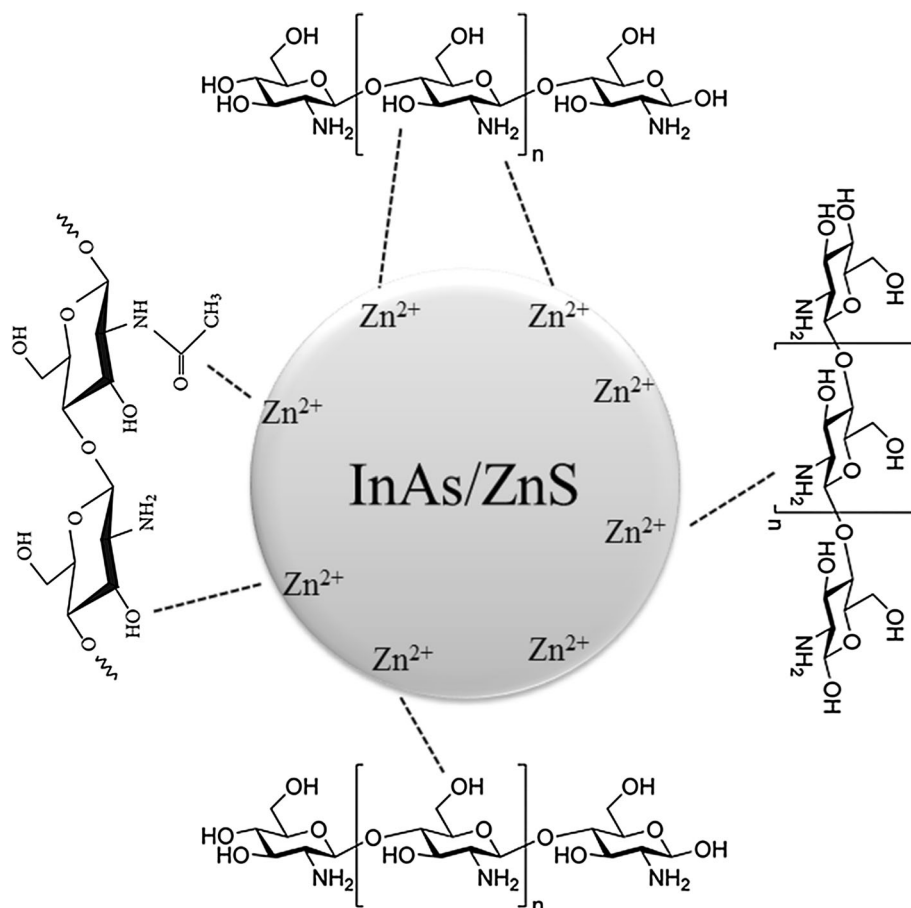

there are two types of particles—larger and smaller ones, all with irregular shape. The smaller ones can be found on the surface of the larger, but they are also scattered among the particles. Using electron energy-dispersive X-ray (EDX) mapping, it was found that the bigger ones can be attributed to InAs and the smaller to ZnS compound. This method also confirms that the system is a mixture composed of individual InAs and ZnS phases. The particle size distribution measured by photon cross-correlation spectroscopy of the InAs/ZnS system is depicted as inset of a SEM micrograph in Fig. 4. The distribution is trimodal with the fractions from 200 to 400 nm, from 400 to 750 nm, and the small fraction from 750 to 1200 nm. The finer fraction can be attributed to the ZnS and the coarser to the InAs system.

### Preparation of chitosan-coated InAs/ZnS nanosuspension

In order to obtain liquid nanosuspension, which is suitable for testing of biological activity and bio-

imaging properties in cancer cells, the second stage of milling was applied. InAs/ZnS particles were subjected to the wet ultra-fine milling process in chitosan solution. The evolution of particle size distribution during milling is shown in Fig. 5. As can be seen, the average particle size (d_{50}) gradually decreased with milling time (from 630 to 487 nm). The largest particles, with the size above 1 μm, disappeared as a consequence of milling. After 240 min of milling, the particles were only in nano-range. By a subsequent centrifugation of the sample, it was possible to affect the parameter d_{50} further, and at 13,000 rpm, the average size of 310 nm was obtained. The colloid suspension prepared by this way was stable, and the particles did not settle down.

Relevant information on how chitosan protects the particles of InAs/ZnS from agglomeration and ensures the stability of the system can be obtained by the ZP measurements. Their values were recorded in the pH range from 3 to 9 (Fig. 6). The sample of pure InAs dispersed in distilled water (InAs–H_2O) was positively charged at lower values of pH. The
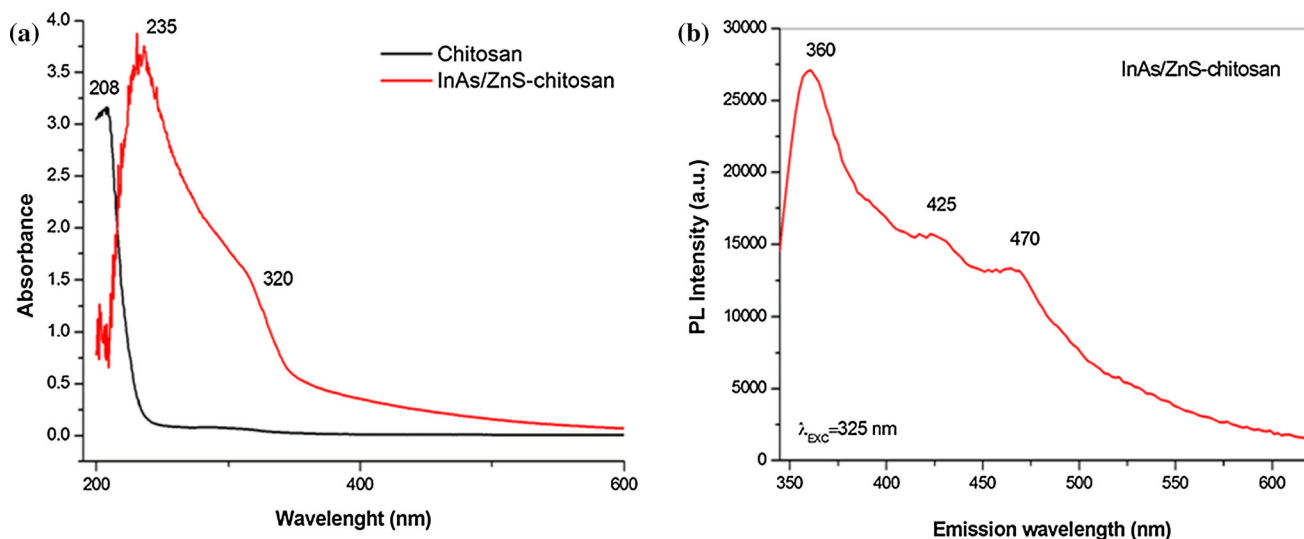
Figure 9 **a** UV–Vis spectra of pure chitosan (*black line*) and chitosan-coated InAs/ZnS nanocrystals (*red line*), **b** PL spectrum of chitosan-coated InAs/ZnS nanocrystals.
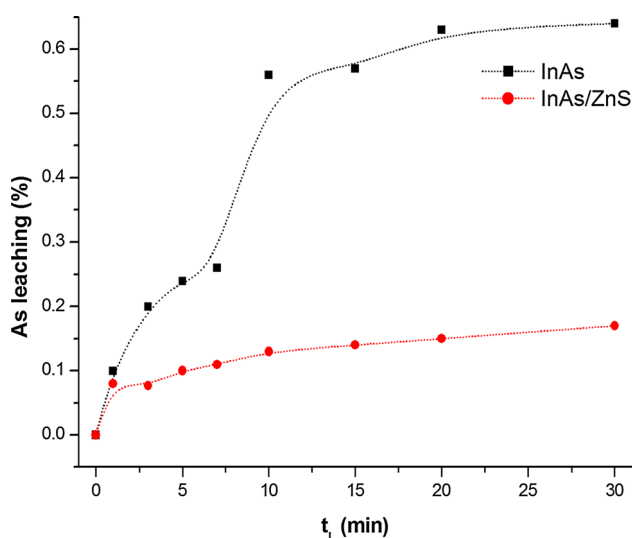
Figure 10 Arsenic leaching from InAs and InAs/ZnS nanocrystals (0.9 % NaCl solution, t_L = 30 min, T_L = 36.5 °C).

maximum value of ZP (+52 mV) was obtained at pH 4. The isoelectric point (IEP) was reached at pH 4.9. Above this point, with increasing amount of a base, the particles acquire more negative charge (up to −35 mV at pH 9). In the case of InAs/ZnS sample diluted in distilled water (InAs/ZnS-H_2O), the values of ZP in the range of pH 4.5–9 were shifted to more positive values in comparison to sample InAs–H_2O. The sample is positively charged in the almost whole measured pH range, and the IEP was detected at pH 8.8. This shift is connected with the presence of Zn(II)

ions in ZnS and their transfer from the sample surface into the solution.

After the milling of InAs/ZnS sample in the environment of chitosan, the values of ZP were shifted to the even more positive areas in a comparison with the samples diluted in distilled water (up to +61 mV at pH 3), into the more stable area. In the case of pure chitosan, the highest value of ZP was also obtained at pH 3 with the ZP value +97 mV. The IEP was reached at pH 8. The same identification of neutral charge of chitosan was also documented in paper [27]. Chitosan is a cationic polymer, with pKa ∼6.5, which is insoluble in water at neutral pH, at which the majority of amines from the molecule are deprotonated. At acidic pH, it is positively charged and it becomes water soluble [28]. The coating of InAs/ZnS nanocrystals by chitosan has led to high positive values of ZP and consequently to their better stability.

The local microenvironment and possible interaction between InAs/ZnS particles and chitosan were studied in detail by FTIR spectroscopy. The spectrum of the pure chitosan, used in our experiments, is depicted in Fig. 7a. The absorption peak at 3358 cm^{-1} is attributed to NH stretching vibration, which overlaps with the vibration of OH hydroxyl group from the carbohydrate ring. The peak at 2876 cm^{-1} represents the symmetric or the asymmetric CH_2 stretching vibration attributed to pyranose ring. The peaks at 1649 and 1583 cm^{-1} correspond to the carbonyl C=O stretching of the amide group (amide I
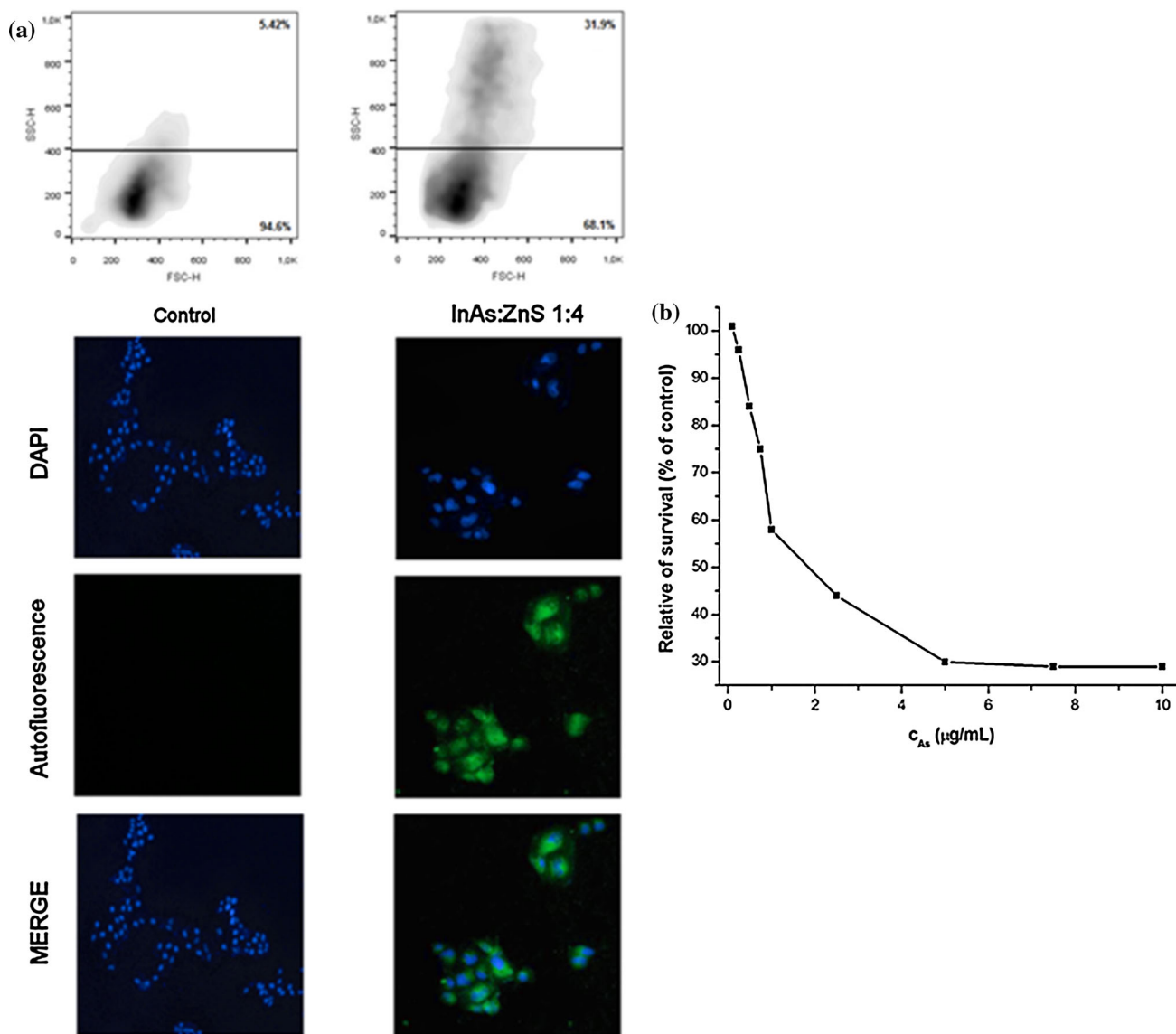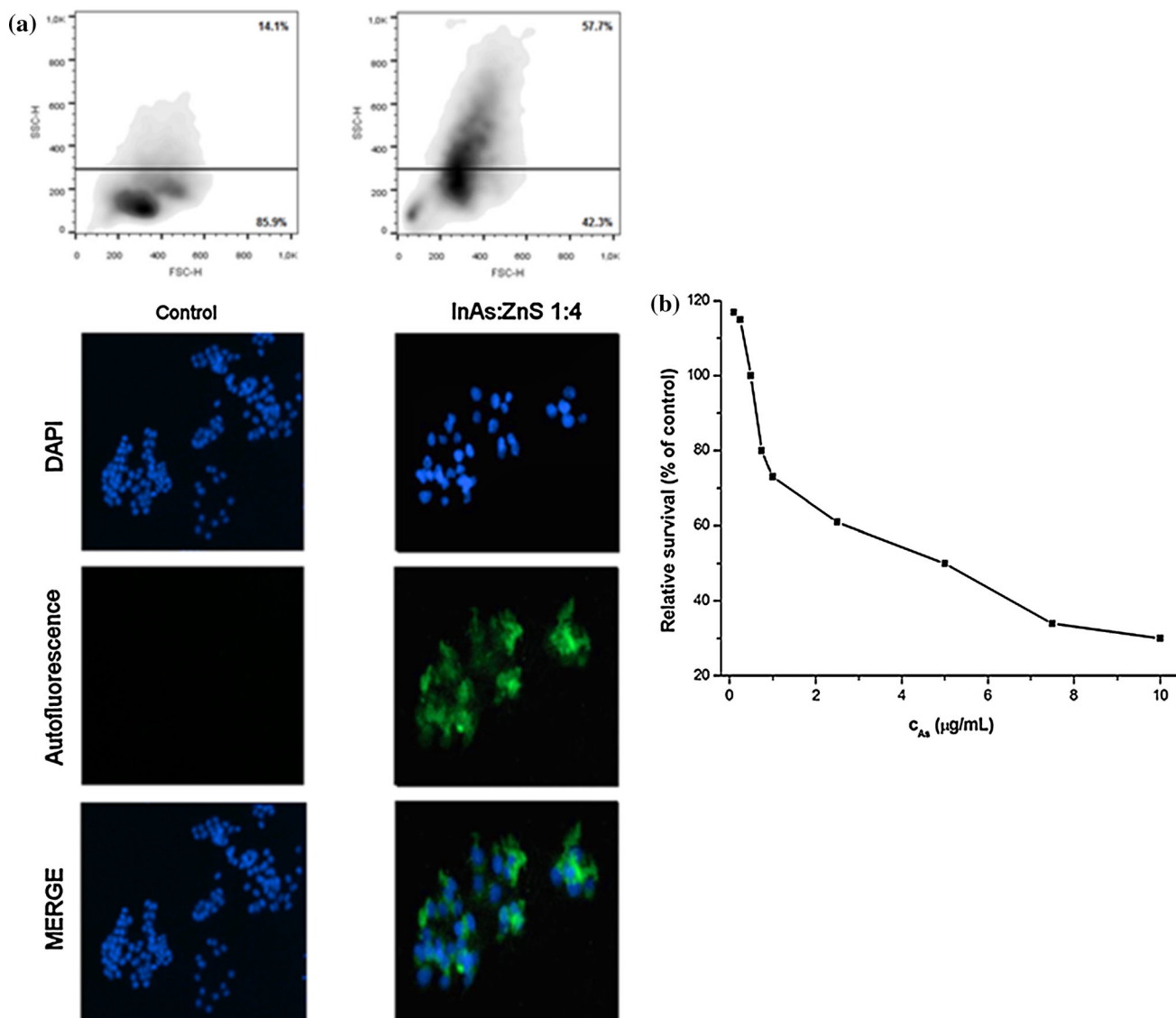
Figure 11 **a** Flow cytometry and fluorescence microscopy analysis, **b** relative survival of Caco-2 cells after their treatment with chitosan-coated InAs/ZnS nanocrystals.

band) and the N–H bending vibrations in amide group (amide II band) and of the deacetylated primary amine-NH₂, respectively. The amide I and amide II bands originate from chitin and deacetylated primary amine from chitosan. The absorption peaks at 1419 and 1316 cm^{-1} are attributed to the OH and CH vibrations in the ring. The 1372 cm^{-1} peak represents the C–H bond vibrations of the methyl group present in the amide group. The C–N stretching and N–H in-plane bending in the amide group (amide III band) are evidenced by the peak present at 1264 cm^{-1}. The absorptions between 1180 and 840 cm^{-1} indicate the C–O stretching vibrations in

chitosan. Concretely, the peak at 1064 cm^{-1} is associated with the C3–OH vibration in the secondary alcohol and one present at 1027 cm^{-1} with the C6–OH vibration in the primary alcohol. These amine, amide, and hydroxyl groups are the most reactive sites of chitosan and are involved in the interactions with the ambient cations and anions [29–33].

After conjugation of the InAs/ZnS nanoparticles with chitosan, several changes were noticed in the characteristic bands of polymer in the FTIR spectra (Fig. 7b–d). These changes denote the possible interaction between these entities. As it can be seen from the figures, the most visible shifts of vibrations occurred
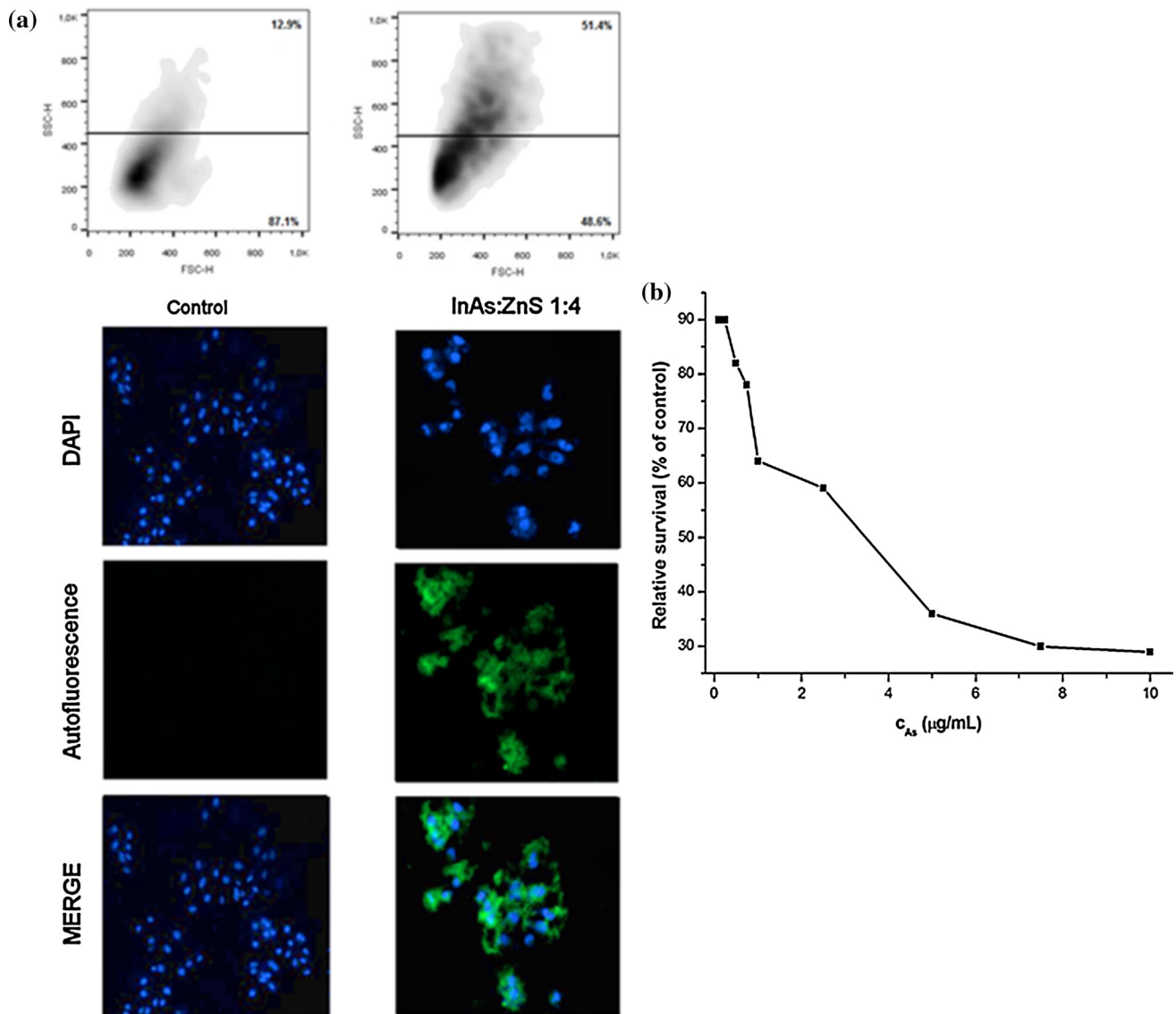
Figure 12 a Flow cytometry and fluorescence microscopy analysis, **b** relative survival of HCT116 cells after their treatment with chitosan-coated InAs/ZnS nanocrystals.

mainly in the hydroxyl group present in the ring (from 1419 and 1316 to 1398 and 1337 cm^{-1}, respectively, Fig. 7b), in the amide I and II bands (from 1649 and 1583, to 1550 cm^{-1}, respectively, Fig. 7c) and in the secondary and primary alcohol vibrations (from 1064 cm^{-1} for C3–OH and 1027 cm^{-1}, for C6–OH to 1059 cm^{-1}, and 1020 cm^{-1}, respectively, Fig. 7d). According to ZP measurements, the Zn(II) ions, present at the surface of InAs/ZnS particles, are responsible for the obtained positive values. The schematic illustration of the possible interaction between chitosan and InAs/ZnS nanoparticles is depicted in Fig. 8.

The UV–Vis spectrum of 0.1 % chitosan solution (Fig. 9a, black line) showed the characteristic

absorption below 220 nm [34], revealing the presence of this polymer. In the case of InAs/ZnS particles milled in this environment (red line), the red shift of the chitosan peak (at 235 nm) and the appearance of a new broad absorption band between 280 and 350 nm with the maximum at 320 nm can be seen. This is associated with the first excitonic transition indicating the presence of ZnS nanocrystals and their synthesis within the 'quantum confinement regime' [35]. The nanoparticles are blue-shifted compared to bulk ZnS with absorption at 343 nm [24]. The obtained absorption peaks indicate the existence of a chemical bond between chitosan and InAs/ZnS nanoparticles [36].

Figure 13 a Flow cytometry and fluorescence microscopy analysis, **b** relative survival of HeLa cells after their treatment with chitosan-coated InAs/ZnS nanocrystals.

The PL spectrum of chitosan-coated InAs/ZnS nanocrystals was measured with the excitation wavelength 325 nm in the region 350–700 nm (Fig. 9b). In this region, the observed peaks show a typical emission of ZnS nanocrystals. The PL consists of a strong emission peak at 360 nm (3.4 eV) and weaker peaks at 425 nm (2.9 eV) and 470 nm (2.6 eV). The emission peak at 360 nm is attributed to the band edge. The wavelength region from 400 nm to 550 nm is primarily associated with point defects, such as vacancies and interstitial ions and also surface states [37, 38]. According to the energy level diagrams reported by Wageh et al. [37], the emission band at 425 nm

observed in the spectrum is associated with sulfur and interstitial zinc ions states. The band present at 470 nm may be assigned to surface states. It is assumed that all defects in nanocrystals may be generated as a consequence of the high-energy milling.

Biological activity

Dissolution of arsenic from InAs and InAs/ZnS nanocrystals

The dissolution of toxic arsenic ions from the InAs and InAs/ZnS nanocrystals is illustrated in Fig. 10.
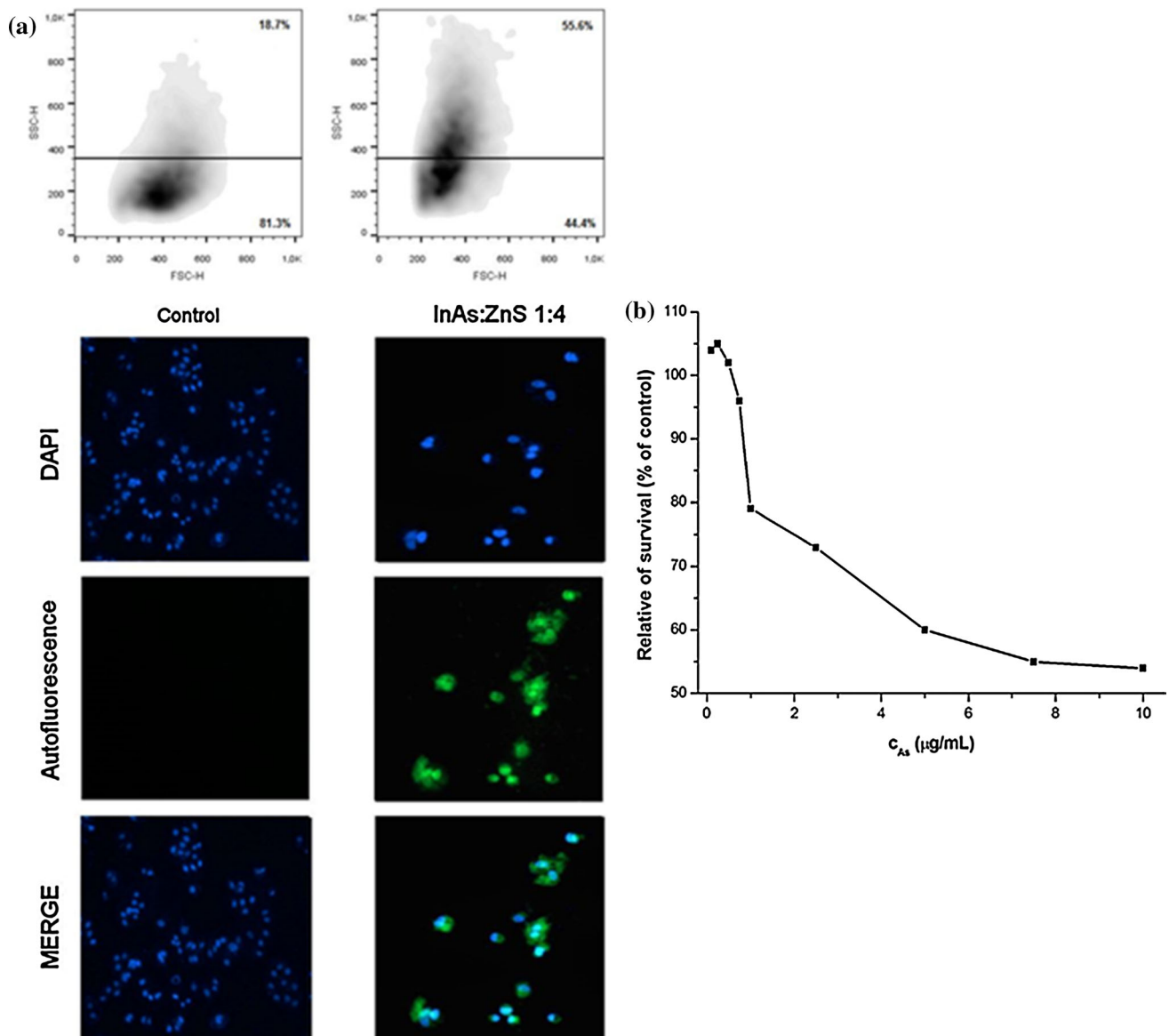
Figure 14 **a** Flow cytometry and fluorescence microscopy analysis, **b** relative survival of MCF7 cells after their treatment with chitosan-coated InAs/ZnS nanocrystals.

The leaching experiments were performed in a physiological medium used in medicine for the intravenous management (0.9 % NaCl solution), for 30 min at human body temperature ($T_L = 36.5$ °C). The highest arsenic leakage was attained for the pure InAs nanocrystals (up to 0.64 %). On the other hand, the dissolution of this toxic element from the mixed InAs/ZnS nanocrystals was considerably lower (0.17 %). In this case, the coating (albeit partial) of ZnS particles on the surface of InAs hinders the leaching of arsenic into the solution, what is very important from the environmental and the toxicity point of view. The similar phenomena were observed also in [39, 40], where the effect of preventing cadmium leakage was achieved in the case of the mixed CdS/ZnS nanocrystals and CdS/ZnS film catalyst, respectively.

In vitro studies

For in vitro tests of chitosan-coated InAs/ZnS nanocrystals, four cancer cell lines, namely Caco-2, HCT116, HeLa, and MCF7, have been applied. In order to study the in vitro behavior of the

nanoparticles, the methods of fluorescence microscopy and flow cytometry were applied. The fluorescence microscope images of the four different cancer cell lines cultivated with InAs/ZnS nanocrystals ($c_{As} = 0.5\ \mu g/mL$) for 72 h as well as flow cytometry analysis showing the granularity are given in Figs. 11, 12, 13, and 14a. For the microscopy analysis, the cell nuclei were stained with DAPI, and the images of the nanocrystals autofluorescence were acquired sequentially and then combined using instrument analysis software (merge).

From the microscopic point of view, it can be seen that the nanocrystals have evident fluorescent properties (see comparison of autofluorescence of control- and InAs/ZnS-treated cells). The nanocrystals passed through the cell membrane, entered into cytoplasm, and surrounded the nucleus (Figs. 11, 12, 13, 14a bottom). In many cells, the nucleus was observed as a distinct object with nanocrystals outlining it, as is shown on the merged pictures. Similar observations were found also in the case of TiO$_2$ and silver nanoparticles [41, 42].

In the flow cytometry analysis (Figs. 11, 12, 13, 14a top), the forward and the side scatter of detectors (FSC-H and SSC-H) are proportional to the cells' size and to their granularity, respectively. When looking at these parameters in the case of control, Caco-2 and HCT116 cancer cells are small in size with poor granularity. HeLa cells are also small, but they are more granular in comparison to previous ones. From the studied cell lines, MCF7 cells are the largest and the most granular. When applying InAs/ZnS nanosuspension, obvious changes can be seen in these two characteristics similarly as in [43, 44]. The cells granularity was rapidly increased in all cases, as a consequence of cellular uptake of the nanoparticles into the cytoplasm.

The metabolic activity of the four cancer cell lines after their exposition toward the InAs/ZnS nanocrystals was also pursued. The results are depicted in Figs. 11, 12, 13, and 14b. The introduction of InAs/ZnS nanocrystals brought about the visible changes. The relative viability of the cells was sharply decreasing with the increasing of arsenic concentration. Moreover, the cells are very sensitive to these nanocrystals, because even a low arsenic concentration (approx. 1 $\mu g/mL$) causes the cell death; hence, these nanocrystals can be considered as toxic. At the concentration of arsenic equal to 7.5 $\mu g/mL$, only 30–50 % of cells survived.

According to these observations, it can be concluded that the studied nanosuspension has fluorescent properties and in perspective it could be used in bio-imaging applications. However, InAs/ZnS nanocrystals seem to be highly toxic and require serious toxicity studies in the future.

Conclusions

In the first step, InAs/ZnS nanocrystals were prepared by mechanosynthesis in a dry mode. Their structural and morphological properties were studied. The system consists of mixed InAs and ZnS nanocrystals with sizes of 45 ± 15 and 2 ± 1 nm, respectively. As a consequence of aggregation, which comes into existence during milling, the particles with the sizes from 200 to 1200 nm are composed of several nanocrystals. In the next step, these particles were subjected to the wet ultra-fine milling in chitosan solution to obtain stable suspension, suitable for the in vitro study of their metabolic activity on the selected cancer cell lines. Such prepared suspension shifted the ZP values from incipient stability to good stability area as a consequence of cationic nature of chitosan.

Using FTIR spectroscopy, it was determined that the chemical interaction between zinc ions from InAs/ZnS and amine, amide, and hydroxyl groups from chitosan takes place. The combination of InAs with ZnS nanocrystals is very beneficial from the environmental point of view. The arsenic concentration in the physiological solution after leaching of InAs/ZnS was four times lower in comparison to the leaching of pure InAs. The ZnS particles partially cover the surface of InAs and hinder the arsenic dissolution. The nanocrystals exhibit fluorescent properties, due to which it is possible to study their distribution in the cells. The results have shown that they entered into the cytoplasm and surrounded the nucleus. The granularity and the metabolic activity of the cells were strongly influenced. Moreover, this sample seems to be very toxic. Therefore, it is strongly recommended before its future application in the field of bio-imaging to perform a detailed toxicity study.

References

[1] Yang MJ, Wang FC, Yang CH, Bennett BR, Do TQ (1996) A composite quantum well field-effect transistor. Appl Phys Lett 69:85–87

[2] Zimmer JP, Kim SW, Ohnishi S, Tanaka E, Frangioni JV, Bawendi MG (2006) Size series of small indium arsenide-zinc selenide core-shell nanocrystals and their application to in vivo imaging. J Am Chem Soc 128:2526–2527

[3] Allen PM, Liu WH, Chauhan VP, Lee J, Ting AY, Fukumura D et al (2010) InAs(ZnCdS) quantum dots optimized for biological imaging in the near-infrared. J Am Chem Soc 132:470–471

[4] Choi HS, Ipe BI, Misra P, Lee JH, Bawendi MG, Frangioni JV (2009) Tissue- and organ-selective biodistribution of NIR fluorescent quantum dots. Nano Lett 9:2354–2359

[5] Kumar C (2010) Semiconductor nanomaterials. Wiley, Weinheim

[6] Dash M, Chiellini F, Ottenbrite RM, Chiellini E (2011) Chitosan—a versatile semi-synthetic apolymer in biomedical applications. Prog Polym Sci 36:981–1014

[7] Jayakumar R, Menon D, Manzoor K, Nair SV, Tamura H (2010) Biomedical applications of chitin and chitosan based nanomaterials—a short review. Carbohydr Polym 82:227–232

[8] Fan HL, Wang LL, Zhao KK, Li N, Shi ZJ, Ge ZG et al (2010) Fabrication, mechanical properties, and biocompatibility of graphene-reinforced chitosan composites. Biomacromolecules 11:2345–2351

[9] Lillo CR, Romero JJ, Portoles ML, Diez RP, Caregnato P, Gonzalez MC (2015) Organic coating of 1–2 nm-size silicon nanoparticles: effect on particle properties. Nano Res 8:2047–2062

[10] Rivero PJ, Urrutia A, Goicoechea J, Zamarreno CR, Arregui FJ, Matias IR (2011) An antibacterial coating based on a polymer/sol–gel hybrid matrix loaded with silver nanoparticles. Nanosc Res Lett 6:1

[11] Nilsson PT, Eriksson AC, Ludvigsson L, Messing ME, Nordin EZ, Gudmundsson A et al (2015) In-situ characterization of metal nanoparticles and their organic coatings using laser-vaporization aerosol mass spectrometry. Nano Res 8:3780–3795

[12] Balaz P, Achimovicova M, Balaz M, Billik P, Cherkezova-Zheleva Z, Criado JM et al (2013) Hallmarks of mechanochemistry: from nanoparticles to technology. Chem Soc Rev 42:7571–7637

[13] Zyryanov VV, Ponomareva VG, Lavrova GV (2006) Preparation, structure, and electrical conductivity of calcium-antimonate-based materials. Inorg Mater 42:410–417

[14] Soiron S, Rougier A, Aymard L, Tarascon JM (2001) Mechanochemical synthesis of Li–Mn–O spinels: positive electrode for lithium batteries. J Power Sources 97–8:402–405

[15] Hallmann S, Fink MJ, Mitchell BS (2011) The mechanochemical formation of functionalized semiconductor nanoparticles for biological, electronic and superhydrophobic surface applications. In: Lu K, Manjooran N, Radovic M, Medvedovski E, Olevsky EA, Li C, Singh G, Chopra N, Pickrell G (eds) Advances in Nanomaterials and Nanostructures, Vol 229. John Wiley & Sons, Inc., Hoboken, NJ. doi:10.1002/9781118144602.ch13

[16] Senna M, Myers N, Aimable A, Laporte V, Pulgarin C, Baghriche O et al (2013) Modification of titania particles for photocatalytic antibacterial activity via a colloidal route with glycine and subsequent annealing. J Mater Res 28:354–361

[17] Balaz P, Balaz M, Caplovicova M, Zorkovska A, Caplovic L, Psotka M (2014) The dual role of sulfur-containing amino acids in the synthesis of IV–VI semiconductor nanocrystals: a mechanochemical approach. Faraday Discuss 170:169–179

[18] Bujnakova Z, Balaz P, Caplovicova M, Caplovic L, Kovac J, Zorkovska A (2015) Mechanochemical synthesis of InAs nanocrystals. Mater Lett 159:474–477

[19] Serrano J, Cantarero A, Cardona M, Garro N, Lauck R, Tallman RE et al (2004) Raman scattering in beta-ZnS. Phys Rev B 69:014301

[20] Arguello CA, Rousseau DL, Porto SPS (1969) First-order Raman effect in wurtzite-type crystals. Phys Rev 181:1351

[21] Schneider J, Kirby RD (1972) Raman scattering from ZnS polytypes. Phys Rev B 6:1290

[22] Ebisuzaki Y, Nicol MJ (1972) Raman spectrum of hexagonal zinc sulfide at high pressures. J Phys Chem Solids 33:763–766

[23] Brafman O, Mitra SS (1968) Raman effect in wurtzite- and zinc-blende-type ZnS single crystals. Phys Rev 171:931

[24] Li T, Gao L, Lei W, Guo L, Yang T, Chen Y et al (2013) Raman study on zinc-blende single InAs nanowire grown on Si (111) substrate. Nanosc Res Lett 8:1–7

[25] Cheetham KJ, Carrington PJ, Krier A, Patel II, Martin FL (2012) Raman spectroscopy of pentanary GaInAsSbP narrow gap alloys lattice matched to InAs and GaSb. Semicond Sci Technol 27:015004

[26] Alim KA, Fonoberov VA, Balandin AA (2005) Origin of the optical phonon frequency shifts in ZnO quantum dots. Appl Phys Lett 86:053103

[27] Bajaj G, Van Alstine WG, Yeo Y (2012) Zwitterionic chitosan derivative, a new biocompatible pharmaceutical excipient, prevents endotoxin-mediated cytokine release. PLoS One 7:e30899

[28] Bowman K, Leong KW (2006) Chitosan nanoparticles for oral drug and gene delivery. Int J Nanomed 1:117–128

[29] Ramanery FP, Mansur AAP, Mansur HS (2013) One-step colloidal synthesis of biocompatible water-soluble ZnS quantum dot/chitosan nanoconjugates. Nanoscale Res Lett 8:512. doi:10.1186/1556-276X-8-512

[30] Pawlak A, Mucha A (2003) Thermogravimetric and FTIR studies of chitosan blends. Thermochim Acta 396:153–166

[31] Bhattarai SR, Kc RB, Kim SY, Sharma M, Khil MS, Hwang PH et al (2008) N-hexanoyl chitosan stabilized magnetic nanoparticles: implication for cellular labeling and magnetic resonance imaging. J Nanobiotechnol 6:1

[32] Ahmad T, Bae H, Iqbal Y, Rhee I, Hong S, Chang Y et al (2015) Chitosan-coated nickel-ferrite nanoparticles as contrast agents in magnetic resonance imaging. J Magn Magn Mater 381:151–157

[33] Salehizadeh H, Hekmatian E, Sadeghi M, Kennedy K (2012) Synthesis and characterization of core-shell Fe_3O_4–gold–chitosan nanostructure. J Nanobiotechnol 10:1

[34] Kumirska J, Czerwicka M, Kaczynski Z, Bychowska A, Brzozowski K, Thoming J et al (2010) Application of spectroscopic methods for structural analysis of chitin and chitosan. Mar Drugs 8:1567–1636

[35] Brus LE (1984) Electron–electron and electron–hole interactions in small semiconductor crystallites: the size dependence of the lowest excited electronic state. J Chem Phys 80:4403–4409

[36] Viswanath R, Naik HSB, Somalanaik YKG, Neelanjeneallu PKP, Harish KN, Prabhakara MC (2014) Studies on characterization, optical absorption, and photoluminescene of yttrium doped ZnS nanoparticles. J Nanotechnol 2014:8

[37] Wageh S, Ling ZS, Xu-Rong X (2003) Growth and optical properties of colloidal ZnS nanoparticles. J Cryst Growth 255:332–337

[38] Chen R, Li DH, Liu B, Peng ZP, Gurzadyan GG, Xiong QH et al (2010) Optical and excitonic properties of crystalline ZnS nanowires: toward efficient ultraviolet emission at room temperature. Nano Lett 10:4956–4961

[39] Balaz P, Bujnakova Z, Dutkova E, Balaz M, Zorkovska A, Kovac J et al (2015) Mixed core CdS@ZnS nanocrystals: synthesis, cadmium dissolution and cancer cell management. In: Rene ER, Bhattarai S, Nancharaiah YV, Lens PNL (eds) 4th international conference on research frontiers in chalcogen cycle science and technology. Delft. pp 7–11

[40] Wang X, Li XY (2014) Photocatalytic hydrogen generation with simultaneous organic degradation by a visible light-driven CdS/ZnS film catalyst. Mater Sci Eng B 181:86–92

[41] Zucker RM, Massaro EJ, Sanders KM, Degn LL, Boyes WK (2010) Detection of TiO_2 nanoparticles in cells by flow cytometry. Cytom Part A 77A:677–685

[42] Zucker RM, Daniel KM, Massaro EJ, Karafas SJ, Degn LL, Boyes WK (2013) Detection of silver nanoparticles in cells by flow cytometry using light scatter and far-red fluorescence. Cytom Part A 83:962–972

[43] Bancos S, Tsai D-H, Hackley V, Weaver JL, Tyner KM (2012) Evaluation of viability and proliferation profiles on macrophages treated with silica nanoparticles in vitro via plate-based, flow cytometry, and coulter counter assays. ISRN Nanotechnol 2012:11

[44] Xu A, Chai YF, Nohmi T, Hei TK (2009) Genotoxic responses to titanium dioxide nanoparticles and fullerene in gpt delta transgenic MEF cells. Part Fibre Toxicol 6:1